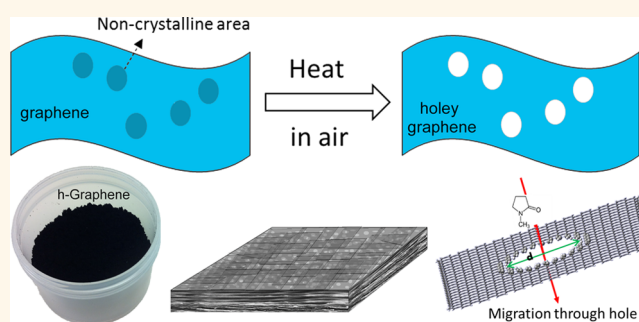


# Scalable Holey Graphene Synthesis and Dense Electrode Fabrication toward High-Performance Ultracapacitors

Xiaogang Han,<sup>†</sup> Michael R. Funk,<sup>\*,§</sup> Fei Shen,<sup>†</sup> Yu-Chen Chen,<sup>†</sup> Yuanyuan Li,<sup>†</sup> Caroline J. Campbell,<sup>||</sup> Jiaqi Dai,<sup>†</sup> Xiaofeng Yang,<sup>†</sup> Jae-Woo Kim,<sup>||</sup> Yunlong Liao,<sup>||,#</sup> John W. Connell,<sup>§</sup> Veronica Barone,<sup>⊥</sup> Zhongfang Chen,<sup>#</sup> Yi Lin,<sup>\*,||,\*</sup> and Liangbing Hu<sup>†,\*</sup>

<sup>†</sup>Department of Materials Science and Engineering, University of Maryland, College Park, Maryland 20742, United States, <sup>‡</sup>Department of Applied Science, The College of William and Mary, Williamsburg, Virginia 23185, United States, <sup>§</sup>Mail Stop 226, Advanced Materials and Processing Branch, NASA Langley Research Center, Hampton, Virginia 23681, United States, <sup>||</sup>National Institute of Aerospace, Hampton, Virginia 23666, United States, <sup>⊥</sup>Department of Physics and Science of Advanced Materials Program, Central Michigan University, Mount Pleasant, Michigan 48859, United States, and <sup>#</sup>Department of Chemistry, Institute for Functional Nanomaterials, University of Puerto Rico, Rio Piedras Campus, San Juan, Puerto Rico 00931

**ABSTRACT** Graphene has attracted a lot of attention for ultracapacitor electrodes because of its high electrical conductivity, high surface area, and superb chemical stability. However, poor volumetric capacitive performance of typical graphene-based electrodes has hindered their practical applications because of the extremely low density. Herein we report a scalable synthesis method of holey graphene (h-Graphene) in a single step without using any catalysts or special chemicals. The film made of the as-synthesized h-Graphene exhibited relatively strong mechanical strength, 2D hole morphology, high density, and facile processability. This scalable one-step synthesis method for h-Graphene is time-efficient, cost-efficient, environmentally friendly, and generally applicable to other two-dimensional materials. The ultracapacitor electrodes based on the h-Graphene show a remarkably improved volumetric capacitance with about 700% increase compared to that of regular graphene electrodes. Modeling on individual h-Graphene was carried out to understand the excellent processability and improved ultracapacitor performance.



**KEYWORDS:** scalable synthesis · facile processability · holey graphene · dense graphene electrode · ultracapacitor · supercapacitor · volumetric capacitance

Graphene is one of the most promising ultracapacitor materials for high-power and high-energy density due to its chemical stability, electric properties, and high theoretical surface area.<sup>1–3</sup> However, two-dimensional (2D) sheets such as graphene tend to aggregate and restack due to van der Waals attraction during the electrode fabrication process, leading to reduced ionic access to the surfaces and thus a low capacitance in practice. To overcome the restacking problem, a great deal of research is presently being conducted to design high-porosity graphene electrodes. These include (1) the manipulation of individual graphene sheet morphology, such as making “crumpled” or “curved” shapes so that artificial porosity is created around each layer;<sup>4</sup> (2) the employment of spacers

such as carbon nanotubes in graphene films to control the graphene–graphene layer distance,<sup>5,6</sup> and (3) the preparation of three-dimensional (3D) porous structures, such as graphene foam and aerogel made of reduced graphene oxide,<sup>7–10</sup> activated graphene-based carbons,<sup>11–13</sup> macroporous graphene frameworks,<sup>9</sup> sponge-like graphene,<sup>14</sup> etc. All the methods above can lead to improved accessibility of electrolytes and ions to the graphene surface, which results in a very high capacitance per weight ( $C_{\text{weight}}$  in F/g). However, these porous electrodes have a low mass density ( $\rho$  in g/L), leading to a low capacitance per volume ( $C_{\text{volume}}$  in F/L) which can be calculated from  $C_{\text{volume}} = C_{\text{weight}} \times \rho$  at the electrode level. In fact, a good volumetric performance of graphene electrodes,  $C_{\text{volume}}$  is arguably

\* Address correspondence to binghu@umd.edu, yi.lin@nianet.org.

Received for review May 14, 2014 and accepted July 31, 2014.

Published online 10.1021/nn502635y

© XXXX American Chemical Society

more essential than gravimetric performance,  $C_{\text{weight}}$  for practical applications.

It has been demonstrated that pristine graphene is not permeable to gas species and metal ions.<sup>15,16</sup> Therefore, the tortuosity for ion transport across the graphene plane is infinite, which greatly hinders the ion accessibility for high-performance ultracapacitors. Holey graphenes have been demonstrated before by a few groups, including us.<sup>17</sup> It refers to graphene sheets with plenty of 2D nanoholes distributed on it.<sup>17–22</sup> These holey graphenes could lead to excellent ion transport across the graphene plane and ultimately access to the inner electrode surfaces. Previous methods, however, either are not scalable or involve the use of toxic or hazardous chemicals. Herein, we describe a scalable, single-step synthetic method for holey graphene (denoted as h-Graphene hereinafter) without any catalysts or chemicals (except for air as the oxidant), using commercially available graphene (Vorbeck, by thermally exfoliation method)<sup>23</sup> as the sole starting material. The as-synthesized h-Graphene was found to be much easier to process into a much denser and stronger film than the commercial graphene (denoted as graphene in this work) which forms a brittle film under the same processing conditions. High-density electrodes are a prerequisite for the improvement of volumetric performance in an ultracapacitor with all-graphene electrodes. As shown in this work, the unique properties of h-Graphene electrodes enable notably larger volumetric capacitance than the graphene electrodes.

## RESULTS AND DISCUSSION

The h-Graphene sheets were synthesized by controlled heating of the graphene powder in air. Figure 1a illustrates the scalable one-step synthesis process.

The noncrystalline spots (point or vacancy defects)<sup>24</sup> on the starting graphene basal planes react with oxygen in hot air (typically  $<500\text{ }^{\circ}\text{C}$ ), leaving holes on the sheets. From thermogravimetric analysis (TGA, Figure S1 in Supporting Information), the highlighted temperature region ( $430\text{--}480\text{ }^{\circ}\text{C}$ ) was the threshold of graphene weight loss and thus was selected for h-Graphene synthesis. This synthesis is robust and can be scaled up easily without any special chemicals or catalysts. The digital photo in Figure 1b shows the h-Graphene products in bulk quantities. The scale-up of the reaction is only limited by the available amount of starting graphene material and the size of the heating unit (*e.g.*, open-ended tube furnaces or air ovens).

Surprisingly, the Raman spectra of the as-synthesized h-Graphene samples suggested their comparable or even improved graphitic crystallinity, relative to the starting graphene. As shown in Figure 1c, the Raman spectrum profile of h-Graphene obtained by heating at  $480\text{ }^{\circ}\text{C}$  for 3 h in air (denoted as  $480\text{ }^{\circ}\text{C}/3\text{ h}$ ) is nearly identical to that of the starting graphene, but the D-to-G ratio (disorder/graphene, ratio of D band centered at  $1333\text{ cm}^{-1}$  to G peak at  $1593\text{ cm}^{-1}$ ) somewhat decreased. This was mainly due to the moderate oxidation temperatures that were used for holey graphene synthesis in this study. In the selected temperature range,  $\text{sp}^2$  carbons (contributing to the G peak) in the graphitic region on the graphene sheets remained stable, while the  $\text{sp}^3$  carbons (contributing to the D band) in the defective region were susceptible to oxidative removal (*i.e.*, gasification).<sup>25,26</sup> Meanwhile, we used micro-Raman with a laser beam size of  $2\text{ }\mu\text{m}$  for the measurement. As a result, it is possible to observe an increased fraction of  $\text{sp}^2$  carbons locally and thus a decreased D-to-G ratio from the measurement.

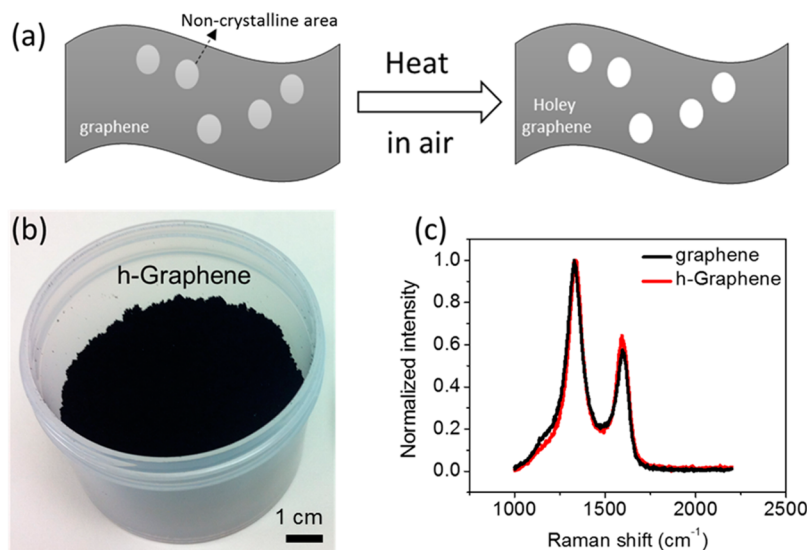


**Figure 1.** (a) Schematic of the scalable synthesis of the h-Graphene sheets, (b) digital photo of the as-synthesized h-Graphene powder in bulk, and (c) Raman spectra comparison for h-Graphene obtained from  $480\text{ }^{\circ}\text{C}/3\text{ h}$  and the starting graphene.

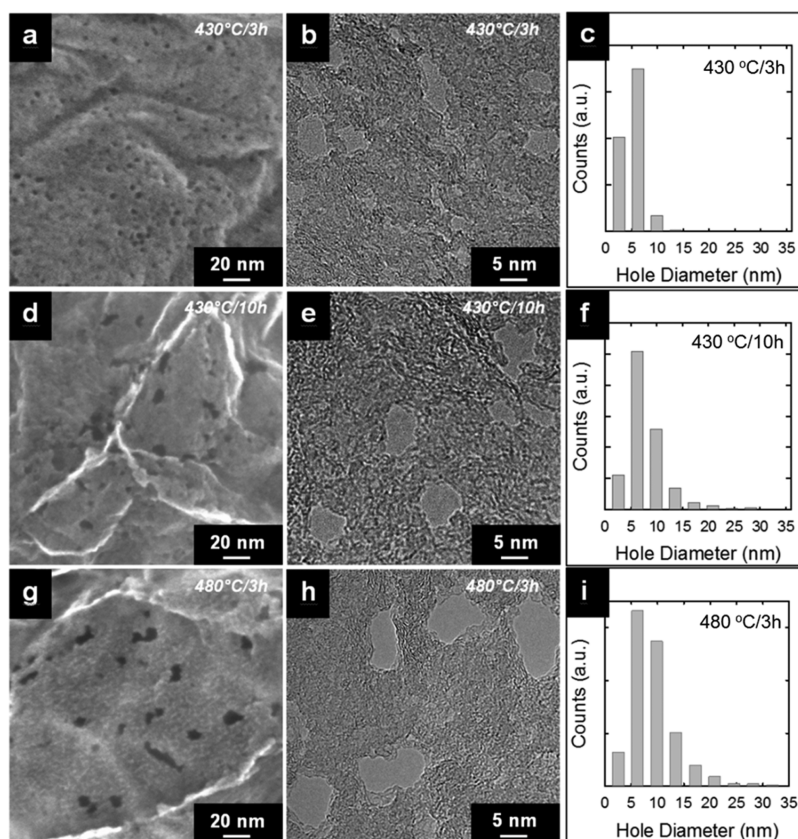


**Figure 2.** Typical SEM (a,d,g) and TEM (b,e,h) images and the corresponding hole diameter distribution statistics (c,f,i, from multiple SEM images) for the h-Graphene samples prepared under different experimental conditions: (a–c) 430 °C/3 h, (d–f) 430 °C/10 h, and (g–i) 480 °C/3 h.

The key to the one-step reaction is to control the extent of partial air oxidation of the graphene sheets. The size, morphology, and density of the holes in the h-Graphene were dependent upon the reaction conditions including heating rate, temperature, and hold time. For the convenience of concept demonstration, the samples reported here are all from a moderate heating rate of  $\sim 10$  °C/min with holding at a set temperature for a certain period of time. To directly observe the holes, a high-resolution scanning electron microscope (Hitachi S-5200 field-emission SEM at 30 kV) and high-resolution transmission electron microscope (JEOL 2100 TEM at 200 kV) were applied. In Figure 2 are shown SEM (left column) and TEM images. Obviously, the h-Graphene samples exhibited a large amount of holes that penetrated through the thicknesses of the graphene layers, while the surfaces of the starting graphene sheets were found to be typically intact (Figure S2 in Supporting Information).<sup>17</sup> Statistical analysis of multiple SEM images acquired at different locations of the h-Graphene specimen of 430 °C/3 h indicated that the average hole diameter was 5.2 nm with a hole surface density of  $1.78 \times 10^3 \mu\text{m}^{-2}$  (Figure 2c). In comparison, the use of higher reaction temperature or longer hold time yielded h-Graphene sheets with larger holes and reduced hole surface density. For example, the average hole diameters for

the h-Graphene obtained from 430 °C/10 h and 480 °C/3 h were 8.0 and 9.2 nm, with hole surface densities of  $0.63 \times 10^3$  and  $0.45 \times 10^3 \mu\text{m}^{-2}$ , respectively (Figure 2f,i). The pore sizes of the starting graphene and h-Graphene samples were characterized *via* the Brunauer–Emmett–Teller and Barret–Joyner–Halenda (BET/BJH) method, respectively, and the pore sizes of h-Graphene thus calculated are unambiguously larger than that of the starting graphene (Figure S3 in Supporting Information). Due to the moderate hole size and distribution (Figure 2f), the h-Graphene samples treated at 430 °C/10 h were selected for more extensive evaluation in ultracapacitor electrode tests presented in the following sections.

Although some holes in the lower-magnification SEM images appeared to be irregularly shaped, HR-TEM images revealed that the 2D nanohole edges were in fact quite smooth locally, likely due to the slow oxidation processes. The irregular shapes might be directly related to the shapes of the intrinsic oxidation-vulnerable regions on the starting graphene sheets. Consistent with the partial oxidation, the oxygen content obtained from X-ray photoelectron spectra (XPS) of the h-Graphene samples gradually increased with the increase of hold temperature and duration (Figure S4 in Supporting Information). From the fitted XPS curves for C 1s, it seems possible that the

newly created edges in the holes were enriched with oxygen functional groups, such as  $-\text{COO}-$ ,  $-\text{C}-\text{O}-$ , and  $-\text{C}=\text{O}$  (Figure S5 and Table S1 in Supporting Information), which was further supported by FT-IR results (Figure S6 in Supporting Information). The increased oxygen-containing groups improved the wettability of polar solvents on h-Graphene films, which was confirmed through contact angle measurement (Figure S7 in Supporting Information). Both *N*-methyl-2-pyrrolidone (NMP) and the ionic liquid 1-ethyl-3-methylimidazolium bis(trifluoroethylsulfonyl)imide (EMI:TFSI) totally wetted the h-Graphene film surface (contact angles  $<5^\circ$ ), while the starting graphene film exhibited contact angles of  $5-10^\circ$  for the same liquids (movies M1–M4 in Supporting Information).

In our previously reported Ag-catalyzed partial graphene oxidation for holey graphene preparation,<sup>17</sup> the hole size was strongly related to the size of the Ag nanoparticles that were in direct contact with the graphitic surface and catalyzed the carbon gasification. Therefore, the distribution of hole sizes in those sheets spanned a much broader range (from a few nm to over 100 nm). For the catalyst-free method reported here, the range of hole sizes was typically in a narrower domain ( $\sim 5-20$  nm for the samples reported here). The above characterization results strongly suggest that the holes first originated from the oxidation/gasification of the most vulnerable carbons on the graphene surface, which should be point or vacancy surface defects. The propagation of the holes from the defect sites depended on the surrounding local carbon network. Further reaction with higher temperature or longer duration resulted in holes of larger sizes due to the continued oxidation of the existing hole edges.

“Pitch formation” on the surface of highly oriented pyrolytic graphite (HOPG) by direct air oxidation was first reported in the 1980s<sup>27</sup> and extensively studied *via* scanning tunneling microscopy (STM) in the 1990s.<sup>28–30</sup> Oxidation of mechanically exfoliated graphene was also studied in detail.<sup>31</sup> The graphene layers in HOPG and those from mechanical exfoliation were typically of much higher crystallinity than the graphene sheets used here and therefore exhibited much more regular pitch shapes (spherical or hexagonal). It can thus be envisioned that graphene sheets from different preparation methods will have different crystallinity and yield h-Graphene sheets with various hole sizes and shapes. Such partial graphene oxidation can potentially be optimized by choosing a starting graphene that produces h-Graphene with the best combination of properties. The method reported herein is highly versatile and noninvasive. Other than the powdery samples reported here, this procedure should be generally applicable to various forms of graphene, including films (“paper”), vertical arrays, substrate-supported graphene (*e.g.*, mechanical exfoliation, chemical vapor deposition,

solution-casting, varied printing graphene, *etc.*), and even graphene oxide and other 2D materials.

h-Graphene exhibited excellent processing advantages for making dense films which is critical for many applications. In our experiment, a procedure of vacuum filtration, predrying, pressing, and drying was applied to make film electrodes for ultracapacitors (see the Methods section). In brief, the as-obtained h-Graphene powder was first dispersed in NMP solvent by bath sonication for 3 h. As a control, regular graphene electrodes were also made using the starting graphene powder with the same procedure. NMP is a well-known solvent for solution-based exfoliation of graphite.<sup>32,33</sup> Here, NMP is used to disperse graphene and h-Graphene. Interestingly, during the sonication, the h-Graphene powder was found to disperse much more quickly than graphene, which is likely due to both the easier access of solvent molecules to h-Graphene powder through the 2D nanoholes and thorough wettability of NMP on h-Graphene (Figure S7 and movie M2 in Supporting Information).

Furthermore, the h-Graphene suspension readily formed a relatively strong film, while the starting graphene sample formed a fragile film. Figure 3a shows the digital photos of both the h-Graphene and graphene filtration films peeled off from the anodized aluminum oxide (AAO) filters after experiencing identical predrying conditions. The h-Graphene film appeared dark gray and unbroken (left). In contrast, the graphene film was black and cracked into several strips during the evaporation process, indicating a better film formation property of the h-Graphene suspension. Good mechanical strength is an important attribute for film electrode processing. In order to improve the mechanical strength further, the films were subjected to an applied pressure of  $7.6 \times 10^4$  psi for 1 min followed by drying at  $110^\circ\text{C}$  for 6 h. To quantify the mechanical strength, tensile tests were performed. As shown in Figure 3b, the h-Graphene film did not fracture until the stress gets to  $7.8\text{ MPa}/(\text{g}/\text{cm}^3)$  corresponding to  $\sim 1.6\%$  strain. The Young's modulus for the h-Graphene film was calculated to be about  $693\text{ MPa}/(\text{g}/\text{cm}^3)$ . In sharp contrast, it was not possible to perform the tensile test on the graphene films because they would break during specimen loading. Clearly, the mechanical strength of h-Graphene film was much better than that of the graphene film, further indicating the attractive features of h-Graphene for application as an electrode.

Figure 3c shows the cross-sectional SEM images for the h-Graphene and graphene films. The thicknesses of the two films were strikingly different, but impressively, the mass areal densities of the two films were kept about the same ( $\sim 0.31\text{ mg}/\text{cm}^2$ ) by design *via* controlling the solution volume and concentration for filtration. The h-Graphene film displays a thickness of  $2.6\ \mu\text{m}$ , about 80% thinner than the graphene film

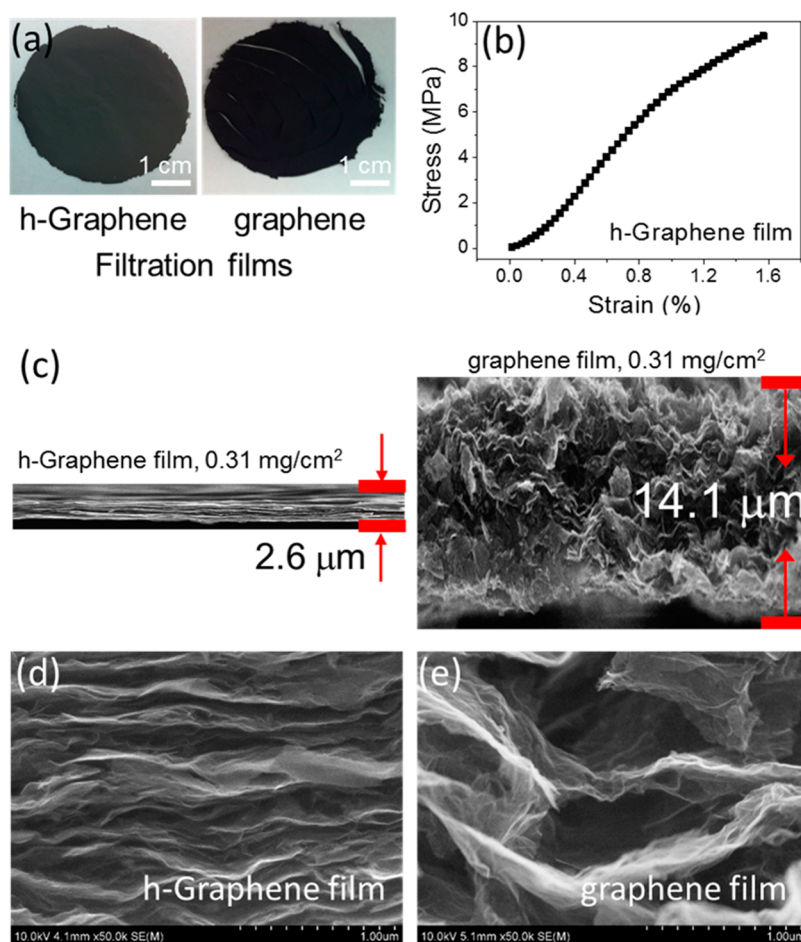


**Figure 3.** (a) Digital photos of h-Graphene and graphene filtration films. The graphene film is cracked during the drying process. (b) Mechanical tensile test result for the h-Graphene film. (c) Cross-sectional SEM images for h-Graphene (left) and graphene films (right) at equivalent areal mass densities of  $0.31 \text{ mg/cm}^2$ . (d,e) Cross-sectional SEM images with identical magnification for h-Graphene (d) and graphene films (e).

( $14.1 \mu\text{m}$ ), meaning the density of h-Graphene film ( $1.2 \text{ g/cm}^3$ ) was about 6 times that of the graphene film ( $0.2 \text{ g/cm}^3$ ). Figure 3d,e compares the cross-section morphology for the two different films. In the h-Graphene film, the individual sheets were basically arranged layer-by-layer with small wrinkles, forming a densely piled structure with small voids ( $\sim 50 \text{ nm}$ ). In the graphene film, the sheets were arranged randomly, forming a great deal of loose and large pocket-like cavities ( $\sim 1 \mu\text{m}$ ). Thus, the dense arrangement morphology in the h-Graphene film accounts for its better film formation properties, superior mechanical strength, and higher density (mass per volume), compared to the graphene film.

The morphology formation within the h-Graphene filtration film can be correlated to the 2D nanoholes *via* a trap-and-escape mechanism. As shown schematically in Figure 4a,b, during the vacuum filtration, the graphene sheets rapidly migrated to the AAO filter with the fast flowing solvent and inevitably formed many compartments with solvent trapped inside. In the case of intact graphene (Figure 4a), the trapped solvent could not be released quickly and only slowly evaporated

through the limited gaps between sheets in the subsequent predrying/pressing/drying processes. Consequently, large spaces were left in the final film, as shown in Figure 3e. In stark contrast, the 2D nanoholes in h-Graphene sheets facilitated the escape of trapped residual solvent during the processes, forming a tightly packed h-Graphene film (Figure 4b). Just like vacuum filtration, the hydraulic pressing could accelerate the trapped solvent escaping from the graphene holes with the collapse of the graphene compartments leading to a dense film. It can be concluded that the introduction of holes in graphene sheets enabled a densely layered morphology by allowing pathways for solvent molecules to escape, resulting in excellent processability and a high-density film.

It is interesting to determine the minimum hole size on h-Graphene through which migrations of the molecular species are allowed. It can be then evaluated whether the hole size distribution obtained in the experiment would allow the trap-and-escape mechanism, even in the presence of chemical terminations at the hole edges. Thus, we performed QM/MM simulations using the ONIOM method (see computational

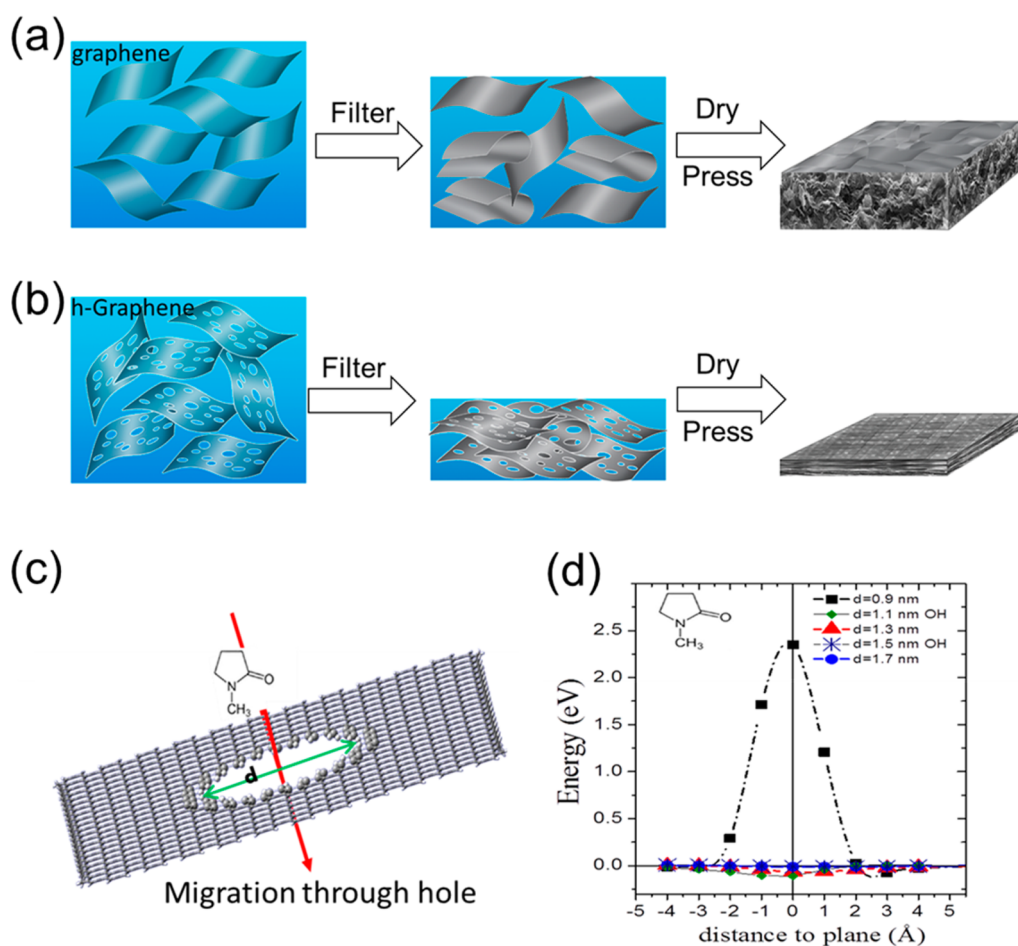


**Figure 4.** (a,b) Schematic illustration of the fabrication of graphene (a) and h-Graphene (b) films by vacuum filtration and drying processes. Due to the escape of solvent through the holes, the h-Graphene filtration film achieves a higher density than that of the graphene filtration film. (c) Scheme of the NMP solvent migrating through holes used in the QM/MM simulations of solvent filtration and evaporation in h-Graphene. (d) Energy barriers obtained from the calculations for the NMP molecule migration through holes of different sizes;  $d$  denotes the diameter of the hole, and OH indicates that the holes are partially terminated by OH groups.

details in the Methods section) of NMP molecules migrating rigidly through holes of different sizes and chemical terminations as shown in Figure 4c. While holes smaller than 0.9 nm present a significant barrier, our simulations, as shown in Figure 4d, demonstrated that NMP solvent molecules can migrate through holes of sizes as small as 1.1 nm. When these holes are partially terminated with oxygen-containing groups, there is a small attractive interaction with NMP which diminishes as the holes become larger. The calculations showed that, based on the size distribution of the holes in our h-Graphene (as shown in Figure 2d–f), NMP molecules are able to easily pass through, thus producing a denser film compared to graphene film where NMP cannot easily escape. These calculations confirmed the relationship between the 2D graphene nanoholes and the combination of properties exhibited by the h-Graphene film and also validated the main mechanism for the trap-and-escape model to allow NMP transport through the holes during the drying process. During drying, the NMP solvent is

evaporated and the gas molecules find an escape mechanism not present in the pristine graphene sample.

These new features of the h-Graphene film, especially the high density, are favorable for ultracapacitors in terms of volumetric performance. To test ultracapacitor properties of the h-Graphene film, a symmetric two-electrode system using coin cells were employed with an ionic liquid EMI:TFSI as the electrolyte. EMI:TFSI has been used as ultracapacitor electrolyte before.<sup>34–36</sup> Different from organic electrolytes containing a solution of a conductive salt dissolved in a solvent, EMI:TFSI self-ionizes and thus no solvation happens, which makes it more straightforward to build up the simulation, though EMI:TFSI may decrease the cell capacitance due to the relative large ion sizes of EMI<sup>+</sup> and TFSI<sup>-</sup>.<sup>37</sup>

Figure 5a shows the cyclic voltammograms (CV) of the h-Graphene ultracapacitor cycled between 0 and 2.5 V at various scan rates. The cell nearly maintained the typical rectangular shape of CVs with a slight distortion possibly due to the oxygen-containing

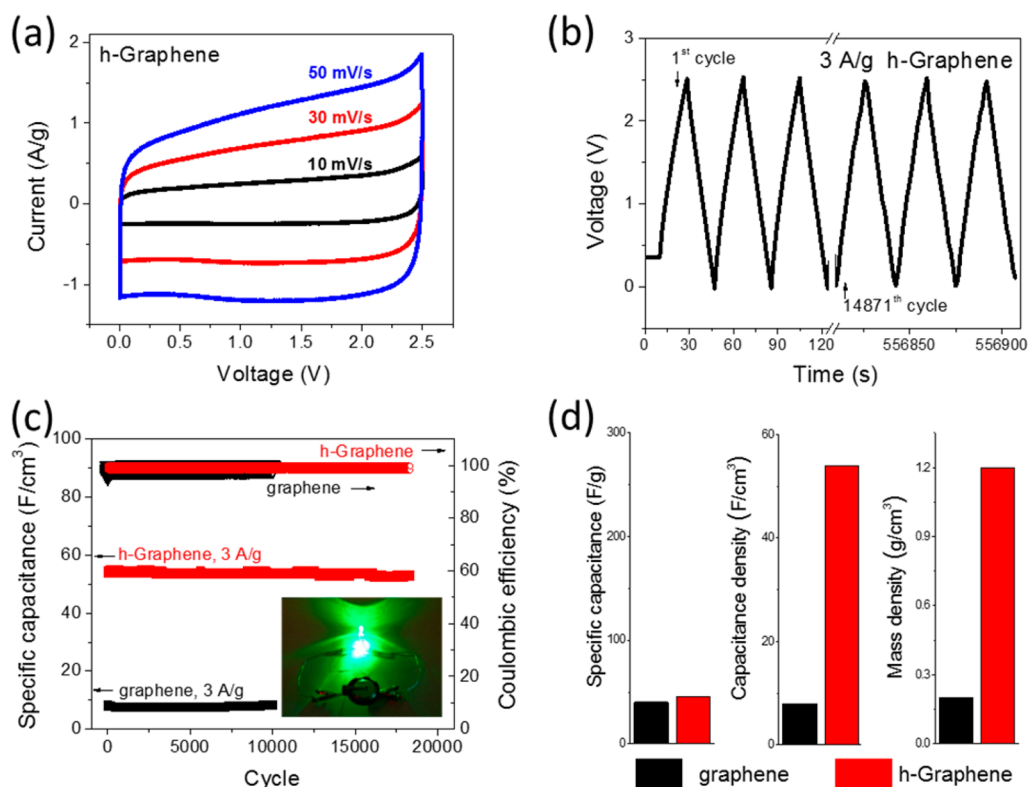


**Figure 5.** Electrochemical properties of h-Graphene film electrodes in a symmetric ultracapacitor. (a) Cyclic voltammogram at various voltage scan rates, (b) galvanostatic charge/discharge curves at a current density of 3 A/g, and (c) cycling performance with Coulombic efficiency. The corresponding results of the graphene film electrode are also shown in (c) in black. (d) Comparison of gravimetric and volumetric capacitance, as well as mass density for the h-Graphene and graphene electrodes. The inset in (c) is a digital photo showing a lighted LED powered by an h-Graphene ultracapacitor assembled in a coin cell.

groups located on the hole edges.<sup>38</sup> These results suggested ideal capacitive behavior of h-Graphene. Figure 5b reveals the linear voltage–time correlation of the galvanostatic charge/discharge curve even after continuous operation for 6 days, characteristic of an electric double-layer capacitance. The specific capacitance per weight and per volume ( $C_{s,w}$ ,  $C_{s,v}$ ) of the full cell can be calculated from galvanostatic charge/discharge curves according to the following equations:

$$C_{s,w}[\text{F/g}] = \frac{I \times \Delta t}{\Delta V \times m} = \frac{Q[\text{mA} \cdot \text{h}] \times 3.6}{\Delta V[\text{V}] \times m[\text{g}]} \quad (1)$$

$$C_{s,v}[\text{F/cm}^3] = C_{s,w}[\text{F/g}] \times \rho[\text{g/cm}^3] \quad (2)$$

where  $I$  is the constant current,  $\Delta t$  the charge or discharge time,  $\Delta V$  the potential range for galvanostatic charge/discharge,  $\rho$  the density of the graphene film electrode,  $m$  the total mass of electrode films in both positive and negative electrodes, and  $Q$  the corresponding charge or discharge capacity. The specific capacitance per volume for the h-Graphene electrode reached 54 F/cm<sup>3</sup> at a current density of 3 A/g.

The h-Graphene symmetric ultracapacitor also exhibited excellent cycling stability at a current density of 3 A/g (Figure 5c). After 10 000 cycles, it retained a high-capacitance density of 53 F/cm<sup>3</sup>, which is about 98% of its initial capacitance with a Coulombic efficiency of

99%. Longer cycling tests show a capacitance retention of 96% after 100 000 cycles (Figure S8 in Supporting Information). The inset in Figure 5c is a digital photo of a LED powered by an h-Graphene ultracapacitor. In stark contrast to the h-Graphene electrodes, the graphene electrodes show an average capacitance of 8 F/cm<sup>3</sup>, only 15% of the h-Graphene's capacitance. The highly increased volumetric capacitance of h-Graphene electrodes over graphene electrodes is mainly ascribed to the ability to fabricate high-density electrodes without sacrificing ion accessibility to h-Graphene surfaces.

To further demonstrate the dense holey graphene film toward ultracapacitors, thicker h-Graphene film electrodes were made through the same processes. They were measured about 9  $\mu\text{m}$  in thickness, 3–4 times thicker than the h-Graphene electrodes discussed above ( $\sim 2 \mu\text{m}$ ). Note that the density of the thick film was almost identical to the thin ones (1.2 g/cm<sup>3</sup>). Similarly, the thick h-Graphene electrodes also exhibited rectangular CV curves, straight time-dependent voltage profiles, and a good cycling stability with high Coulombic efficiency of 99.7%, indicating an excellent capacitive behavior (Figures S9–S11 in Supporting Information). The specific capacitance of the thicker h-Graphene electrodes, however, decreased about 25% from 54 to 41 F/cm<sup>3</sup>. This is expected as there were reports on a

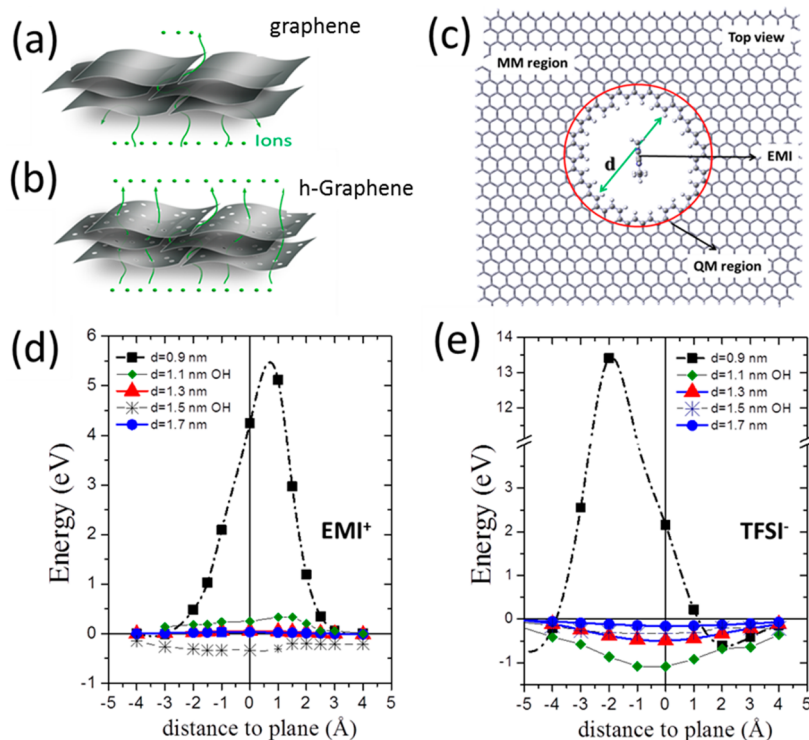


**Figure 6.** (a) Schematic representation of the mechanism of ion migration in graphene and (b) h-Graphene. (c) Model system of h-Graphene utilized for the QM/MM calculations;  $d$  represents the average diameter of the hole and is varied between 0.9 and 1.7 nm. OH in (c) indicates the partial termination of C atoms at the hole edges with OH groups; otherwise, the edges were terminated with H atoms. (d) Relative energies with respect to the molecule at a large distance (10 Å) from the h-Graphene plane for the EMI<sup>+</sup> rigidly migrating through the hole. (e) Relative energies with respect to the molecule at a large distance (10 Å) from the h-Graphene plane for the TFSI<sup>-</sup> rigidly migrating through the hole.

drop in the capacitance by a factor of 2 to 3 when the thickness of the nanoporous carbon electrode increases.<sup>37,39</sup>

Figure 5d shows a comparison of the volumetric and gravimetric capacitance for the two kinds of electrodes with the same mass loading. They both exhibit an almost equivalent specific capacitance (capacitance per weight) under the current conditions (Figure 5d, left), but due to the high density of the h-Graphene film, the volumetric capacitances are dramatically different (Figure 5d, middle). According to eq 2, this effect is mainly explained by the distinct difference in density for the two electrodes (Figure 5d, right). In addition, from the comparison, it can be inferred that the graphene layers in the dense h-Graphene film did not restack significantly as the h-Graphene and graphene electrodes deliver comparable gravimetric capacitances (with the h-Graphene electrode slightly higher). The functional groups distributed on the h-Graphene sheets are likely to reduce the restacking due to the steric repulsion between graphene layers. In electrochemical impedance spectroscopy of h-Graphene electrodes, the diffusion of electrolyte ions was observed between resistance capacitor semicircle and the straight line of whole capacitance region (176 to 6.7 Hz in Figure S12 in Supporting Information). Clearly, the high density of h-Graphene electrodes did not impede ion diffusion.

h-Graphene (here, 430 °C/10 h) showed a somewhat increased BET surface area (658 m<sup>2</sup>/g) from the starting graphene (471 m<sup>2</sup>/g), likely due to the creation of porosity in the bulk sample from the loss of less graphitized carbons, which also contributed to the slight increase of the gravimetric capacitance for the h-Graphene electrodes compared to the graphene electrodes (45 vs 40 F/g) under the experimental conditions.

It is noticed that the value of volumetric capacitance reported here is lower than the ones reported recently.<sup>38,40</sup> A possible reason for the discrepancy with theoretical value of graphene (550 F/g)<sup>41</sup> is the relatively low BET surface area of the starting graphene used in our study (typically 5–15 graphene layers; Figure S13 in Supporting Information). The surface area of a single graphene sheet is 2630 m<sup>2</sup>/g.<sup>2</sup> Thus, the specific capacitance could have been intrinsically limited in both the starting graphene and the h-Graphene electrodes in this work. It is expected that h-Graphene from graphene materials with more exfoliated structures would provide much higher capacitance values.

In addition to the increase of volumetric capacitance, the maximal volumetric energy densities of h-Graphene were about 12 Wh/L at 3 A/g, 6 times that of the starting graphene (~2 Wh/L). With the optimization of the processes (filtration, drying, and pressing)

and the selection of starting graphene, the volumetric performance for h-Graphene can be improved further.

Although the mass density of the h-Graphene film is 5–6 times that of pristine graphene, the ion accessibility is almost as good as that in the pristine one, as shown by the specific capacitance measurement. We additionally set out to investigate the possibility of ionic transport through the holes. Our calculations employed a QM/MM model within the ONIOM scheme similar to that used for the NMP solvent molecules, but in this case, the bulkier EMI<sup>+</sup> and TFSI<sup>-</sup> ions are each allowed to rigidly migrate to the center of the holes. For this migration scheme, and due to the asymmetric nature of the ions involved, we choose the least favorable rigid configuration which will produce the highest barriers due to steric repulsion. In this manner, we ensure that the minimum hole size for easy penetration of both EMI<sup>+</sup> and TFSI<sup>-</sup> ions is found. In Figure 6a,b, a scheme of the ion migration in graphene and h-Graphene is presented, graphically showing the likelihood of ion migration through holes for improved ion diffusion. Figure 6c shows the scheme employed in the QM/MM calculations where the diameter, *d*, as well as the groups terminating the hole edges were varied. The results of these calculations are shown in Figure 6d for EMI<sup>+</sup> and 6e for TFSI<sup>-</sup>. The energy barriers for the EMI<sup>+</sup> can be as large as 5.5 eV for a diameter of 0.9 nm. OH-terminated holes with an average diameter of 1.1 nm present a significantly lower barrier. Such a large energy barrier will make the penetration of ions impossible in practice. However, holes larger than 1.3 nm in diameter allow the rigid migration of EMI<sup>+</sup> without a significant energy barrier.

Similarly, TFSI<sup>-</sup> presents an enormous barrier for holes of 0.9 nm or less caused by steric repulsion. In this case, the chemical nature of the edge termination plays a more important role in stabilizing the structures. For TFSI<sup>-</sup> and partial OH terminations, there is an attractive interaction between h-Graphene and TFSI<sup>-</sup> toward the hole even at hole sizes of 1.1 nm, indicating the possibility of a chemical bond formation. Although

full relaxation of the structures might be needed for finding detailed specific interactions, such as chemical bonds between edge sites and the ions or solvent molecules, our calculations provide an estimation of the minimum hole size that would permit the molecular migration. Consistently, our calculations indicated that holes sizes larger than 1.3 nm will allow penetration of the two ions studied here, and we therefore expect that EMI<sup>+</sup> and TFSI<sup>-</sup> would easily migrate through the holes in the h-Graphene films obtained in our experiments which have significantly larger sizes than 1.3 nm.

## CONCLUSIONS

In summary, we have demonstrated a scalable one-step synthesis of h-Graphene using commercially available graphene with a catalyst-free and chemical-free procedure. The through-thickness nanohole size and distribution could be tuned in the graphene sheets by controlling the heating temperature and exposure duration in air. Importantly, from Raman results, the as-synthesized h-Graphene is observed to maintain or even improve its graphitic crystallinity. As a result of the 2D nanoholes, an h-Graphene film was readily obtained with enhanced mechanical strength, denser microscopic structure, and much higher mass density, in contrast to the film made of graphene without holes. The obtained h-Graphene film demonstrated a remarkably increased volumetric performance and superior cycling stability as ultracapacitor electrodes. A trap-and-escape mechanism and QM/MM calculations elucidated and confirmed the contribution of the 2D nanoholes to enable facile processing and volumetric capacitance improvement for the h-Graphene electrodes. The 2D nanoholes (>1.3 nm) were found to be viable pathways for the access and penetration of solvent NMP molecules as well as electrolyte ions of EMI:TFSI. The scalable and robust synthesis method and the novel properties of h-Graphene presented here greatly advance the practicality of using it as electrodes in ultracapacitors as well as other energy storage technologies.

## METHODS

**Synthesis of h-Graphene.** In a typical reaction, the starting graphene material (200 mg; Vor-X from Vorbeck Materials; grade, reduced 070; lot, BK-77x) was placed in an alumina crucible and heated in air with an open-ended tube furnace (Thermolyne 21100; temperature reported are after calibration) with a ramp rate of ~10 °C/min and held isothermally at the set temperature (typically less than 500 °C) for a given period of time. h-Graphene product was directly obtained upon cooling the reaction.

**Fabrication of h-Graphene Film.** The h-Graphene film was fabricated by vacuum filtration with subsequent drying and pressing. Briefly, the as-synthesized h-Graphene powder (50 mg) was dispersed in NMP (100 mL) with bath sonication for 3 h to prepare the h-Graphene dispersion. The dispersion (10 mL) was vacuum filtered using an AAO filter (Millipore Anodisc 47; 0.2 μm of pore diameter and 47 mm of filter diameter). The obtained

filtration film on the AAO filter was allowed to stand overnight. Usually, the graphene film detached from the AAO filter naturally. Otherwise, the free-standing graphene film could be obtained by carefully scratching the graphene film edge on the AAO filter with fine tips. The free-standing graphene films were punched into disks (3/8 in. diameter) followed by pressing at  $7.6 \times 10^4$  psi for 1 min and drying in oven at 110 °C for 6 h, and then they were transferred to a high-purity Ar-filled glovebox for the coin cell assembly after weighing with a microbalance. The regular graphene films were obtained using the same procedure.

**Material Characterizations.** Micro-Raman analysis was performed using a Horiba Yvon LabRam ARAMIS confocal Raman microscope with a helium neon 10 mW laser excitation source (632.8 nm). The power of the laser beam was adjusted to 0.1 mW with neutral filters for various optical densities. The other parameters for the spectra collection applied on the sample are 2 μm laser beam spot

size, 2 times of acquisition, and 10 s of expose time. By applying these parameters, both the graphene and h-Graphene were not be damaged during the measurement. FT-IR spectra were acquired on a Thermo-Nicolet FT-IR 300 spectrometer equipped with a Thunderdome Swap-Top single reflection attenuated total reflectance module. A Hitachi SU-70 analytical scanning electron microscope was used for the cross-section observation. SEM images were also acquired on a Hitachi S-5200 field-emission SEM system at a typical acceleration voltage of 30 kV. TEM images were obtained using a JEOL 2100 field-emission TEM system at an acceleration voltage of 200 kV. XPS data were collected on a Kratos Axis 165 X-ray photoelectron spectrometer operating in hybrid mode using monochromatic Al K $\alpha$  X-rays (1486.7 eV). Charge neutralization was required to minimize surface charging. BET surface area values were obtained from nitrogen adsorption-desorption isotherms collected using a Quantachrome Nova 2200e surface area and pore size analyzer system. Tensile strength tests were performed using a dynamic mechanical analysis machine (Q800) in tension film mode. Before testing, each sample was cut into a strip of 3 mm  $\times$  20 mm and conditioned for 24 h at 50% humidity at room temperature.

**Cell Assembly and Electrochemical Tests.** Two of the punched h-Graphene or graphene disks (3/8 in. diameter) with identical weight were used as symmetric electrodes without any binder or any extra conductive materials. Typically, the mass of each disk was 0.1 to 0.3 mg. Ionic liquid EMI:TFSI (Iolitec, 99.5%) was utilized as the electrolyte. The ultracapacitors were assembled with two symmetric electrodes in CR2025-type coin cells in an argon-filled glovebox (oxygen content  $\leq$ 0.01 ppm, water content  $\leq$ 0.05 ppm). The electrochemical behavior of the ultracapacitor coin cells was characterized by cyclic voltammetry and galvanometric charge/discharge using a Biologic battery tester (SAS, model 1:VMP3).

**Computational Details.** QM/MM ONIOM calculations were conducted on h-Graphene model systems using the Gaussian 09 package of programs.<sup>42,43</sup> For the high level region (QM), we utilized density functional theory calculations at the B3LYP/6-31G\* level of theory,<sup>44</sup> while the low level region (MM) was modeled using the force field, UFF.<sup>45</sup> Within this approach, the NMP solvent molecule and the electrolyte ions (*i.e.*, EMI<sup>+</sup> and TFSI<sup>-</sup>) were each allowed to rigidly migrate through the center of holes of different sizes and different terminations, including H and OH groups. The sizes of the high-level and low-level regions considered in the calculations are shown in Supporting Information (Figure S14). Energy barriers are obtained as the energy difference between the system with the molecular species at a distance  $h$  from the graphene plane (with  $-4 \text{ \AA} < h < 4 \text{ \AA}$ ) and the energy of the system with  $h = 10 \text{ \AA}$ .

**Conflict of Interest:** The authors declare no competing financial interest.

**Acknowledgment.** The authors thank Dr. W. Cao and Prof. H. Elsayed-Ali at Applied Research Center of Old Dominion University for their experimental assistance in acquiring TEM images. V.B. and L.H. gratefully acknowledge the support from NSF-CBET Grant Nos. 1335944 and 1335979, respectively. Y.L. and J.K. acknowledge the financial support from the Leading Edge Aeronautics Research for NASA (LEARN) program (Grant No. NNX13AB88A). M.F. is supported by the NASA Pathways Intern Employment Program (IEP). C.C. was a Langley Aerospace Research Summer Scholars (LARSS) Program scholar supported by LEARN. Z.C. acknowledges the support by Department of Defense (Grant No. W911NF-12-1-0083) and NASA (Grant Nos. NNX10AM80H and NNX13AB22A). We thank Prof. D. DeVoe, Dr. E. Kendall, and the Maryland Microfluidic Laboratory (MML) for providing access to the goniometer.

**Supporting Information Available:** Additional information on TGA, XPS, FT-IR, HR-TEM, contact angle, BET/BJH, electrochemical impedance spectroscopy characterizations of h-Graphene, longer cycling stability of h-Graphene ultracapacitor electrodes, model system for QM/MM calculations, and movies for contact angle tests are provided. This material is available free of charge via the Internet at <http://pubs.acs.org>.

## REFERENCES AND NOTES

- Li, D.; Kaner, R. B. Graphene-Based Materials. *Science* **2008**, *320*, 1170–1171.
- Stoller, M. D.; Park, S. J.; Zhu, Y. W.; An, J. H.; Ruoff, R. S. Graphene-Based Ultracapacitors. *Nano Lett.* **2008**, *8*, 3498–3502.
- Zhang, L. L.; Zhao, X.; Stoller, M. D.; Zhu, Y. W.; Ji, H. X.; Murali, S.; Wu, Y. P.; Perales, S.; Clevenger, B.; Ruoff, R. S. Highly Conductive and Porous Activated Reduced Graphene Oxide Films for High-Power Supercapacitors. *Nano Lett.* **2012**, *12*, 1806–1812.
- Luo, J.; Jang, H. D.; Huang, J. Effect of Sheet Morphology on the Scalability of Graphene-Based Ultracapacitors. *ACS Nano* **2013**, *7*, 1464–1471.
- Qiu, L.; Yang, X. W.; Gou, X. L.; Yang, W. R.; Ma, Z. F.; Wallace, G. G.; Li, D. Dispersing Carbon Nanotubes with Graphene Oxide in Water and Synergistic Effects between Graphene Derivatives. *Chem.—Eur. J.* **2010**, *16*, 10653–10658.
- Yu, D. S.; Dai, L. M. Self-Assembled Graphene/Carbon Nanotube Hybrid Films for Supercapacitors. *J. Phys. Chem. Lett.* **2010**, *1*, 467–470.
- Niu, Z. Q.; Chen, J.; Hng, H. H.; Ma, J.; Chen, X. D. A Leavening Strategy To Prepare Reduced Graphene Oxide Foams. *Adv. Mater.* **2012**, *24*, 4144–4150.
- Zhang, L.; Zhang, F.; Yang, X.; Long, G. K.; Wu, Y. P.; Zhang, T. F.; Leng, K.; Huang, Y.; Ma, Y. F.; Yu, A.; *et al.* Porous 3D Graphene-Based Bulk Materials with Exceptional High Surface Area and Excellent Conductivity for Supercapacitors. *Sci. Rep.* **2013**, *3*, 1408.
- Choi, B. G.; Yang, M.; Hong, W. H.; Choi, J. W.; Huh, Y. S. 3D Macroporous Graphene Frameworks for Supercapacitors with High Energy and Power Densities. *ACS Nano* **2012**, *6*, 4020–4028.
- Worsley, M. A.; Pauzaskie, P. J.; Olson, T. Y.; Biener, J.; Satcher, J. H.; Baumann, T. F. Synthesis of Graphene Aerogel with High Electrical Conductivity. *J. Am. Chem. Soc.* **2010**, *132*, 14067–14069.
- Zhao, X.; Zhang, L. L.; Murali, S.; Stoller, M. D.; Zhang, Q. H.; Zhu, Y. W.; Ruoff, R. S. Incorporation of Manganese Dioxide within Ultraporous Activated Graphene for High-Performance Electrochemical Capacitors. *ACS Nano* **2012**, *6*, 5404–5412.
- Zhu, Y. W.; Murali, S.; Stoller, M. D.; Ganesh, K. J.; Cai, W. W.; Ferreira, P. J.; Pirkle, A.; Wallace, R. M.; Cychosz, K. A.; Thommes, M.; *et al.* Carbon-Based Supercapacitors Produced by Activation of Graphene. *Science* **2011**, *332*, 1537–1541.
- Kim, T.; Jung, G.; Yoo, S.; Suh, K. S.; Ruoff, R. S. Activated Graphene-Based Carbons as Supercapacitor Electrodes with Macro- and Mesopores. *ACS Nano* **2013**, *7*, 6899–6905.
- Xu, Z. W.; Li, Z.; Holt, C. M. B.; Tan, X. H.; Wang, H. L.; Amirkhiz, B. S.; Stephenson, T.; Mitlin, D. Electrochemical Supercapacitor Electrodes from Sponge-like Graphene Nanoarchitectures with Ultrahigh Power Density. *J. Phys. Chem. Lett.* **2012**, *3*, 2928–2933.
- Jiang, D. E.; Cooper, V. R.; Dai, S. Porous Graphene as the Ultimate Membrane for Gas Separation. *Nano Lett.* **2009**, *9*, 4019–4024.
- Berry, V. Impermeability of Graphene and Its Applications. *Carbon* **2013**, *62*, 1–10.
- Lin, Y.; Watson, K. A.; Kim, J. W.; Baggett, D. W.; Working, D. C.; Connell, J. W. Bulk Preparation of Holey Graphene via Controlled Catalytic Oxidation. *Nanoscale* **2013**, *5*, 7814–7824.
- Zhao, X.; Hayner, C. M.; Kung, M. C.; Kung, H. H. Flexible Holey Graphene Paper Electrodes with Enhanced Rate Capability for Energy Storage Applications. *ACS Nano* **2011**, *5*, 8739–8749.
- Radich, J. G.; Kamat, P. V. Making Graphene Holey. Gold-Nanoparticle-Mediated Hydroxyl Radical Attack on Reduced Graphene Oxide. *ACS Nano* **2013**, *7*, 5546–5557.
- Bai, J. W.; Zhong, X.; Jiang, S.; Huang, Y.; Duan, X. F. Graphene Nanomesh. *Nat. Nanotechnol.* **2010**, *5*, 190–194.

21. Zeng, Z. Y.; Huang, X.; Yin, Z. Y.; Li, H.; Chen, Y.; Li, H.; Zhang, Q.; Ma, J.; Boey, F.; Zhang, H. Fabrication of Graphene Nanomesh by Using an Anodic Aluminum Oxide Membrane as a Template. *Adv. Mater.* **2012**, *24*, 4138–4142.
22. Wang, M.; Fu, L.; Gan, L.; Zhang, C. H.; Rummeli, M.; Bachmatiuk, A.; Huang, K.; Fang, Y.; Liu, Z. F. CVD Growth of Large Area Smooth-Edged Graphene Nanomesh by Nanosphere Lithography. *Sci. Rep.* **2013**, *3*, 1238.
23. Schniepp, H. C.; Li, J. L.; McAllister, M. J.; Sai, H.; Herrera-Alonso, M.; Adamson, D. H.; Prud'homme, R. K.; Car, R.; Saville, D. A.; Aksay, I. A. Functionalized Single Graphene Sheets Derived from Splitting Graphite Oxide. *J. Phys. Chem. B* **2006**, *110*, 8535–8539.
24. Banhart, F.; Kotakoski, J.; Krasheninnikov, A. V. Structural Defects in Graphene. *ACS Nano* **2011**, *5*, 26–41.
25. Nan, H. Y.; Ni, Z. H.; Wang, J.; Zafar, Z.; Shi, Z. X.; Wang, Y. Y. The Thermal Stability of Graphene in Air Investigated by Raman Spectroscopy. *J. Raman Spectrosc.* **2013**, *44*, 1018–1021.
26. Larciprete, R.; Fabris, S.; Sun, T.; Lacovig, P.; Baraldi, A.; Lizzit, S. Dual Path Mechanism in the Thermal Reduction of Graphene Oxide. *J. Am. Chem. Soc.* **2011**, *133*, 17315–17321.
27. Yang, R. T.; Wong, C. Mechanism of Single-Layer Graphite Oxidation—Evaluation by Electron-Microscopy. *Science* **1981**, *214*, 437–438.
28. Chang, H. P.; Bard, A. J. Formation of Monolayer Pits of Controlled Nanometer Size on Highly Oriented Pyrolytic-Graphite by Gasification Reactions As Studied by Scanning Tunneling Microscopy. *J. Am. Chem. Soc.* **1990**, *112*, 4598–4599.
29. Chang, H. P.; Bard, A. J. Scanning Tunneling Microscopy Studies of Carbon Oxygen Reactions on Highly Oriented Pyrolytic-Graphite. *J. Am. Chem. Soc.* **1991**, *113*, 5588–5596.
30. Patrick, D. L.; Cee, V. J.; Beebe, T. P. Molecule Corrals for Studies of Monolayer Organic Films. *Science* **1994**, *265*, 231–234.
31. Liu, L.; Ryu, S. M.; Tomasik, M. R.; Stolyarova, E.; Jung, N.; Hybertsen, M. S.; Steigerwald, M. L.; Brus, L. E.; Flynn, G. W. Graphene Oxidation: Thickness-Dependent Etching and Strong Chemical Doping. *Nano Lett.* **2008**, *8*, 1965–1970.
32. Han, X.; Chen, Y.; Zhu, H.; Preston, C.; Wan, J.; Fang, Z.; Hu, L. Scalable, Printable, Surfactant-Free Graphene Ink Directly from Graphite. *Nanotechnology* **2013**, *24*, 205304.
33. Hernandez, Y.; Nicolosi, V.; Lotya, M.; Blighe, F. M.; Sun, Z. Y.; De, S.; McGovern, I. T.; Holland, B.; Byrne, M.; Gun'ko, Y. K.; et al. High-Yield Production of Graphene by Liquid-Phase Exfoliation of Graphite. *Nat. Nanotechnol.* **2008**, *3*, 563–568.
34. Largeot, C.; Portet, C.; Chmiola, J.; Taberna, P.-L.; Gogotsi, Y.; Simon, P. Relation between the Ion Size and Pore Size for an Electric Double-Layer Capacitor. *J. Am. Chem. Soc.* **2008**, *130*, 2730–2731.
35. Tsai, W.-Y.; Lin, R.; Murali, S.; Zhang, L.; McDonough, J. K.; Ruoff, R. S.; Taberna, P.-L.; Gogotsi, Y.; Simon, P. Outstanding Performance of Activated Graphene Based Supercapacitors in Ionic Liquid Electrolyte from –50 to 80 °C. *Nano Energy* **2013**, *2*, 403–411.
36. Zhang, F.; Tang, J.; Shinya, N.; Qin, L.-C. Hybrid Graphene Electrodes for Supercapacitors of High Energy Density. *Chem. Phys. Lett.* **2013**, *584*, 124–129.
37. Gogotsi, Y.; Simon, P. True Performance Metrics in Electrochemical Energy Storage. *Science* **2011**, *334*, 917–918.
38. Yan, J.; Wang, Q.; Wei, T.; Jiang, L.; Zhang, M.; Jing, X.; Fan, Z. Template-Assisted Low Temperature Synthesis of Functionalized Graphene for Ultrahigh Volumetric Performance Supercapacitors. *ACS Nano* **2014**, *8*, 4720–4729.
39. Chmiola, J.; Largeot, C.; Taberna, P.-L.; Simon, P.; Gogotsi, Y. Monolithic Carbide-Derived Carbon Films for Micro-supercapacitors. *Science* **2010**, *328*, 480–483.
40. Yang, X. W.; Cheng, C.; Wang, Y. F.; Qiu, L.; Li, D. Liquid-Mediated Dense Integration of Graphene Materials for Compact Capacitive Energy Storage. *Science* **2013**, *341*, 534–537.
41. Xia, J. L.; Chen, F.; Li, J. H.; Tao, N. J. Measurement of the Quantum Capacitance of Graphene. *Nat. Nanotechnol.* **2009**, *4*, 505–509.
42. Dapprich, S.; Komaromi, I.; Byun, K. S.; Morokuma, K.; Frisch, M. J. A New ONIOM Implementation in Gaussian98. Part I. The Calculation of Energies, Gradients, Vibrational Frequencies and Electric Field Derivatives. *J. Mol. Struct.: THEOCHEM* **1999**, *461*, 1–21.
43. Vreven, T.; Byun, K. S.; Komaromi, I.; Dapprich, S.; Montgomery, J. A.; Morokuma, K.; Frisch, M. J. Combining Quantum Mechanics Methods with Molecular Mechanics Methods in ONIOM. *J. Chem. Theory Comput.* **2006**, *2*, 815–826.
44. Becke, A. D. Density-Functional Thermochemistry. III. The Role of Exact Exchange. *J. Chem. Phys.* **1993**, *98*, 5648–5652.
45. Rappe, A. K.; Casewit, C. J.; Colwell, K. S.; Goddard, W. A.; Skiff, W. M. Uff, a Full Periodic-Table Force-Field for Molecular Mechanics and Molecular-Dynamics Simulations. *J. Am. Chem. Soc.* **1992**, *114*, 10024–10035.